ACS EARTH AND SPACE CHEMISTRY

Article

Cite This: ACS Earth Space Chem. 2019, 3, 519−530

http://pubs.acs.org/journal/aesccq

Effects of Mn^{2+}, Ni^{2+}, and Cu^{2+} on the Formation and Transformation of Hydrosulfate Green Rust: Reaction Processes and Underlying Mechanisms

Xiaoming Wang,[†] Jing Peng,[†] Xiaoliang Liang,[‡] Mengqiang Zhu,[§] Bruno Lanson,[∥] Lanxin Wang,[†] Xinran Liang,[†] Fan Liu,[†] Wenfeng Tan,[†] and Xionghan Feng*[,†]

[†]Key Laboratory of Arable Land Conservation (Middle and Lower Reaches of Yangtze River), Ministry of Agriculture, College of Resources and Environment, Huazhong Agricultural University, Wuhan 430070, China

[‡]CAS Key Laboratory of Mineralogy and Metallogeny, Guangzhou Institute of Geochemistry, Chinese Academy of Sciences, Guangzhou 510640, P. R. China

[§]Department of Ecosystem Science and Management, University of Wyoming, Laramie, Wyoming 82071, United States

[∥]Univ. Grenoble Alpes, Univ. Savoie-Mont Blanc, CNRS, IRD, IFSTTAR, ISTerre, F-38000 Grenoble, France

Supporting Information

ABSTRACT: Green rusts (GRs), which are important intermediate phases during Fe^{2+} oxidation, are commonly associated with various metal cations during their crystallization in soils and sediments, but the effects of these foreign metal cations on the formation of GRs and on their subsequent transformation to Fe (hydr)oxides remain unclear. In the present study, the effects of Mn^{2+}, Ni^{2+}, and Cu^{2+} on the evolution processes of hydrosulfate green rust (GR2) are documented under various conditions and the mechanisms leading to cation incorporation in the reaction products are determined. The rates of GR2 formation and of its transformation to Fe (hydr)oxides both decrease in the order of Cu^{2+} > Ni^{2+} > Mn^{2+} and increase with increasing metal cation concentration. During GR2 crystallization, a small fraction of foreign metal cations is structurally incorporated in GR2 by replacing Fe^{2+}, and their amount in the mineral follows the order of Cu^{2+} > Ni^{2+} > Mn^{2+}. Under all conditions, the final reaction products are a mixture of lepidocrocite and goethite; a slow oxidation rate of mineral Fe^{2+} and a strong catalytic effect of surface Fe^{2+} both facilitate the goethite formation from GR2, reversely, favorable to lepidocrocite formation. Additionally, the three cations possess different speciation and distribution in lepidocrocite and goethite: Mn exists mainly as Mn(III) and probably minor Mn(II)−Mn(III) molecular clusters and occurs mainly in the mineral interior by isomorphic substitution or coated by the Fe (hydr)oxides crystals; Ni is present as Ni(II) and uniformly distributed in the newly formed minerals by either isomorphic substitution or surface adsorption; finally, Cu is mainly sorbed at the mineral surface as Cu(II) with minor Cu(I). These cations may thus be structurally incorporated in Fe oxides in the order of Mn(III) > Ni(II) > Cu(II). These new insights into the interaction between GR2 and trace metal cations improve our understanding of Fe oxide crystallization processes and of the environmental geochemical behavior of associated metal cations in redox alternating soils and sediments.

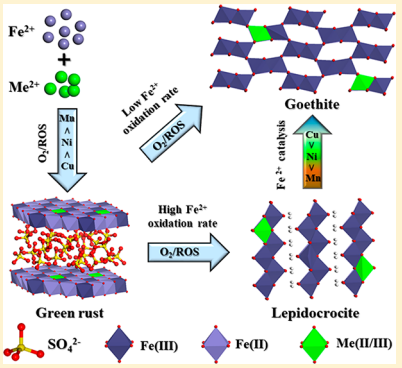

KEYWORDS: *Green rust, lepidocrocite, goethite, Mn^{2+}, Ni^{2+}, Cu^{2+}, formation, transformation*

INTRODUCTION

Green rusts (GRs) are widely distributed in anoxic environments, such as subsurface soils, sediments, and groundwater, and represent an important intermediate phase during the formation and transformation of various iron oxides.[1−3] The precipitation and transformation of GRs are key processes of the Fe cycle, which regulates and influences the speciation and bioavailability of Fe and the environmental geochemical behaviors of various associated elements.[1,2,4,5] The structure of GRs consists of $Fe^{II, III}$ octahedral layer and interlayer anions alternately, belonging to the class of layered double hydroxides (LDHs). During the process of $Fe^{2+}/Fe(OH)_2$ oxidation into GRs, some Fe^{II} cations from the octahedral layer are oxidized to Fe^{III}, thus inducing a positive charge in the Fe octahedral layer, which needs to be balanced by the interlayer anions (such as Cl^-, SO_4^{2-}, CO_3^{2-}, etc.).[6−8] According to the different arrangement of interlayer anions, GRs can be divided into two types:[6,9] GR1 with planar anions, e.g., Cl^- and CO_3^{2-}, and GR2 with three-dimensional anions, e.g., SO_4^{2-} and

Special Issue: Iron Redox Chemistry and Its Environmental Impact

Received: November 30, 2018
Revised: January 30, 2019
Accepted: February 8, 2019
Published: February 8, 2019

DOI: 10.1021/acsearthspacechem.8b00187
ACS Earth Space Chem. 2019, 3, 519−530

SeO_4^{2-}. Compared to GR1, GR2 usually has a larger crystal size and a smoother particle surface.[10]

Owing to their large surface area and the large amount of structural Fe^{2+}, GRs exhibit strong adsorption capacity and reductive reactivity. They can efficiently reduce Se(VI), Cr(VI), U(VI), and some organic pollutants, thereby changing their speciation and toxicity.[11−15] Additionally, GRs are unstable when exposed to air or in contact with other oxidizing compounds, and they are easily oxidized and transformed into more stable high-valent Fe (hydr)oxides. Transformation mechanisms and reaction products of GRs are closely related to the reaction conditions. For example, during GR1 transformation, oxidation rate of mineral Fe^{2+} is increased by lower pH, lower temperature, or higher dissolved O_2 conditions; as the Fe^{2+} oxidation rate increases, the final products change from magnetite to goethite and to lepidocrocite through a dissolution−oxidation−precipitation (DOP) mechanism.[16] In the presence of increasing concentration of PO_4^{3-}, AsO_4^{3-}, or silicate,[17−20] the transformation mechanisms of GRs transit from DOP to solid-state oxidation (SSO), and reaction products change from well-crystallized goethite and/or lepidocrocite to a mixture of ferric GR (structure similar to that of GR but only containing Fe^{III}), poorly crystalline goethite and/or lepidocrocite, and ferrihydrite.

In addition to the oxyanions, metal cations can react with GRs and thus affect their formation and subsequent transformation. GR2 interlayers can contain monovalent cations in addition to anions and H_2O,[21] interlayer thickness being linearly correlated with the radius of the monovalent cations. Under anaerobic conditions, oxidizing cations such as Ag^+, Au^{3+}, or Cu^{2+} coexisting with GRs suspension can be reduced to their zerovalent forms and simultaneously increase the reduction rate of organic pollutants and nitrate.[22−24] In addition, the presence of Al^{3+} or Cr^{3+} in solution significantly inhibits the growth of GR2 crystals, causing a poor crystallinity and a small particle size.[25,26] Finally, the presence of Mn^{2+} promotes the transformation of GR2 to magnetite,[27] while Al^{3+} significantly accelerates the oxidation of GR2 and promotes the formation of goethite.[26] However, the formation and transformation processes and mechanisms of GRs in the presence of these different metal cations remain unclear.

In southern China, there is a large area of paddy soils contaminated with heavy metals,[28,29] where GRs are common, especially under flooded conditions.[9,30] Additionally, these naturally occurring GRs likely contain trace metal cations, such as Ni^{2+}, Cu^{2+}, and Zn^{2+}.[3,31,32] However, it remains unknown how trace metal cations affect the formation of Fe oxides through Fe^{2+} oxidation, i.e., oxidation of $Fe^{2+}/Fe(OH)_2$ to metastable GRs and then to stable iron (hydr)oxides, and how the metal cations are possibly accumulated in the iron oxides. In the present study, three divalent cations, i.e., Mn^{2+}, Ni^{2+}, and Cu^{2+}, which have different hydrolysis constants, redox properties, and surface complexation constants with iron oxides, are chosen to determine the effects of foreign metal cation nature and concentration, and of the stage when they are introduced (at the beginning or after GR formation) on the formation and transformation of hydroxysulfate green rust (abbreviated as GR2). The effect of suspension pH during GR2 transformation is also examined.

During the formation of GR2 and its subsequent transformation to stable Fe oxides, the suspension pH and Eh were monitored, Fe^{2+} and cation concentration in the solution and in the solid were measured, and the solids in wet paste were immediately characterized using fast-scanning X-ray diffraction (XRD) to avoid phase transformation during data collection. The final solid products were air-dried and characterized by conventional and synchrotron-based XRD, Fourier transform infrared (FTIR) spectroscopy, and transmission electron microscopy (TEM). The metal cation speciation and spatial distribution in the air-dried final reaction products were determined using X-ray absorption spectroscopy (XAS) and acidic dissolution kinetics. Results improve our understanding of the formation and transformation pathways of Fe oxides in the presence of trace metal cations, and how these processes affect the fate and transport of the metals in metal-contaminated paddy soils.

MATERIALS AND METHODS

Preparation of GR2. GR2 was synthesized using previously reported methods.[33] Specifically, the synthesis was started by adding 90 mL of 0.127 M $FeSO_4$ to 90 mL of 0.211 M NaOH solution (OH/Fe = 1.66) in a 300 mL reaction cell under stirring at 25 °C.[16] The mixed solution was aerated, and Fe^{II} was accordingly oxidized by atmospheric O_2. The suspension pH was monitored with a pH electrode (Metrohm 6.0280.300) and the redox potential (Eh) with a Pt electrode (Metrohm 6.0451.100), both of which referred to an Ag/AgCl reference electrode. GR2 formation was generally complete when the pH and Eh curves reached their first inflection points.[34,35] Then, GR2 continued to be oxidized in the same reaction setting, to form other Fe oxides. The GR2 transformation was complete when the pH and Eh curves reached the second inflection points or the suspension color remained unchanged.[34,35]

Formation and Transformation of GR2 in the Presence of Mn^{2+}, Ni^{2+}, or Cu^{2+} (System A). In system A, 10 mL of a cation solution ($MnSO_4$, $NiSO_4$, or $CuSO_4$: 2.5 or 10 mM) was quickly mixed with the above initial solution (90 mL of 0.127 M $FeSO_4$ and 90 mL of 0.211 M NaOH), and oxidized by atmospheric oxygen at 25 °C under stirring conditions. The corresponding molar ratios of Fe/Me^{2+} (x = $[Fe_{total}]/[Me^{2+}]$) were 24 and 6. In the control system, the metal solution was replaced with the same concentration of Na_2SO_4. The suspension pH and Eh were monitored during the formation and subsequent transformation of GR2. Additionally, to explore the pH effects on the GR2 transformation, once GR2 formation was complete for the Fe/Mn = 24 system, the suspension pH was controlled at pH 7.3 by adding 1 M NaOH solution using an automatic pH titrator (Metrohm 907).

Transformation of GR2 in the Presence of Mn^{2+}, Ni^{2+}, or Cu^{2+} (System B). When the formation of GR2 in the aforementioned control system (i.e., the Na^+ system with Na_2SO_4) was complete, the reaction cell was closed and flushed with N_2 for ∼40 min to stabilize the GR2 by removing the dissolved O_2. Ten milliliters of the cation solution ($MnSO_4$, $NiSO_4$, or $CuSO_4$) were then added to the GR2 suspension and oxidized under stirring and aerated conditions. This reaction system was defined as system B. The molar ratios were set at 24 and 6 as well, with the same concentration of Na_2SO_4 solution as a comparison. The suspension pH and Eh were monitored as described above.

Solution and Solid Analysis during the Formation and Transformation of GR2. For measuring the Fe^{2+} and other metal concentrations and the XRD analysis, 2.5 mL of

DOI: 10.1021/acsearthspacechem.8b00187
ACS Earth Space Chem. 2019, 3, 519−530

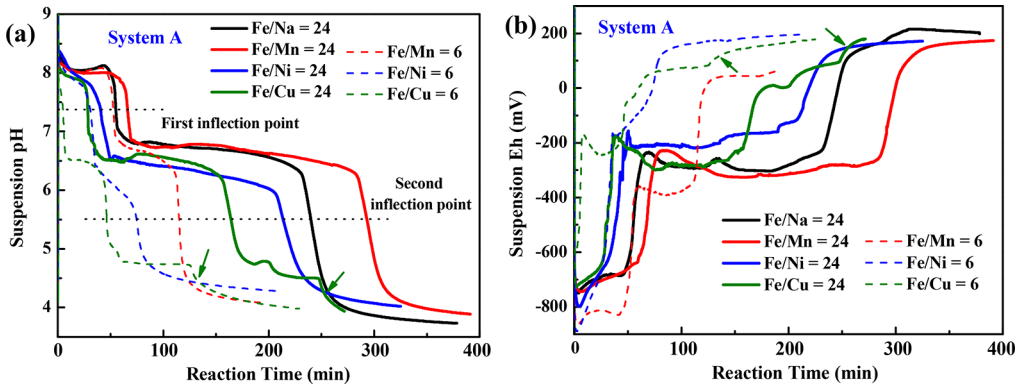

Figure 1. Variation of suspension pH (a) and suspension Eh (b) during the formation and transformation of GR2 in the presence of Mn^{2+}, Ni^{2+}, or Cu^{2+} with Fe/Me^{2+} = 24 or 6 for system A.

suspension was taken from the stirred suspension at time intervals that were defined according to the suspension color and variation of pH/Eh curves. An aliquot of the suspension (0.1 mL) was directly dissolved in 4.9 mL of 5 M H_2SO_4. The supernatant and the solid of the remaining 2.4 mL suspension were separated through 0.22 μm membrane filters, and 0.5 mL of the filtrates was acidified in 4.5 mL of 0.36 M H_2SO_4 to measure the concentrations of dissolved Fe, Mn, Ni, and Cu either with the 1,10-phenanthroline colorimetric method or with atomic absorption spectroscopy (AAS). The Fe^{2+} and cation content in the solid were determined as the concentration differences between the suspension and the supernatant. Meanwhile, the wet paste of the solid deposited on the membrane was immediately measured by XRD. To prevent the oxidation of GR2 during XRD data collection, a thin layer of glycerin was coated on the surface of the reaction products.[36] When the reaction was complete, the final products were quickly centrifuged and washed with deaerated water to prevent the further reaction of Fe^{2+} with atmospheric O_2. Then the solid was vacuum-dried at 40 °C, ground, and stored at 4 °C. The final dried products were characterized by conventional and synchrotron based XRD and quantitative XRD Rietveld analysis, TEM, FTIR spectroscopy, XANES spectroscopy, and XPS.

Acidic Dissolution Kinetics of the Final Products. To decipher the dissolution rate and distribution of cations in the final products, the acidic dissolution kinetics were examined with 100 mg of dried sample dissolved in 250 mL of 4 M HCl solution at 40 °C or 250 mL of 0.2 M ammonium oxalate [$(NH_4)_2C_2O_4$, pH 3] at room temperature and stirring conditions.[37] The sample was completely dissolved in the HCl solution within 2 h, while only poorly crystalline minerals were dissolved in the oxalate solution within 4 h. At the predetermined time intervals, 2.5 mL of suspension was sampled and filtered through a 0.22 μm membrane filter. The cation and Fe concentrations in the filtrate were determined by AAS.

Solid Sample Characterization. XRD measurements were carried out with a Bruker D8 ADVANCE X-ray diffractometer equipped with a LynxEye detector using Ni-filtered Cu Kα radiation (λ = 0.15418 nm). The diffractometer was operated at tube voltage of 40 kV and tube current of 40 mA with a scanning rate of 10°·min^{-1} for the intermediate wet products and 1°·min^{-1} for the final dried products at a step size of 0.02°. To further determine the fraction of lepidocrocite and goethite in the final products, XRD patterns were fitted with a two-phase Rietveld quantitative analysis using the program TOPAS and the crystal-structure models of lepidocrocite (ICSD 27846) and goethite (ICSD 71810).[16] Additionally, in order to better compare the peak intensity and peak position of the final dried products, most samples were also subject to synchrotron based XRD using X-rays of 58.66 keV (λ = 0.2114 Å) at beamline 11-ID-B at the Advanced Photon Source (Argonne National Laboratory). Methods and procedures are detailed in our previous studies.[17,38]

The FTIR spectra of the final dried samples were recorded on a Bruker Vertex 70 spectrophotometer. The samples were mixed very gently with KBr (1% sample weight) in an agate mortar and pelletized. Each sample was measured over the 4000−400 cm^{-1} spectral range with a 4 cm^{-1} resolution in the transmission mode. Thirty-two scans were collected for each sample, and the spectral data were acquired, processed, and analyzed using the OPUS program. The morphology and crystallite size were obtained from TEM analysis (Philips-CM12 and H-7650, Hitachi, both operated at 120 kV). The samples were dispersed in absolute ethanol via sonication, deposited on holey Cu grids, and air-dried prior to TEM imaging. The Mn, Ni, and Cu K-edge XAS of selected samples were collected in fluorescence mode at beamline 1W1B (Beijing Synchrotron Radiation Facility, BSRF).[39] The Combo method was used to determine the fractions of Mn(II), Mn(III), and Mn(IV) in the reaction products,[40] and the accuracy of the average valence is estimated to be ±0.04.

Cu 2p X-ray photoelectron spectra (XPS) of selected dried samples were collected using a VG Multilab2000 X-ray photoelectron spectrometer with a Mg Kα X-ray source (1486 eV). The scans were recorded using the large area mode. Full XPS spectra (1100−5 eV) were collected using a fixed pass energy of 100 eV and an energy step size of 1.0 eV, whereas the narrow scan of Cu 2p has a pass energy of 25 eV and an energy step size of 0.1 eV. The charge effect was corrected by adjusting the binding energy (BE) of C (1s) to 284.6 eV. The spectra were analyzed using the Avantage software. A Shirley-type background was subtracted before deconvolution and fitting.

RESULTS

Suspension pH and Eh during the Formation and Transformation of GR2. For system A, during the formation and transformation of GR2 in the presence of cations, the suspension pH gradually decreases (Figure 1a), while the suspension Eh generally shows an increasing trend, with a

DOI: 10.1021/acsearthspacechem.8b00187
ACS Earth Space Chem. 2019, 3, 519−530

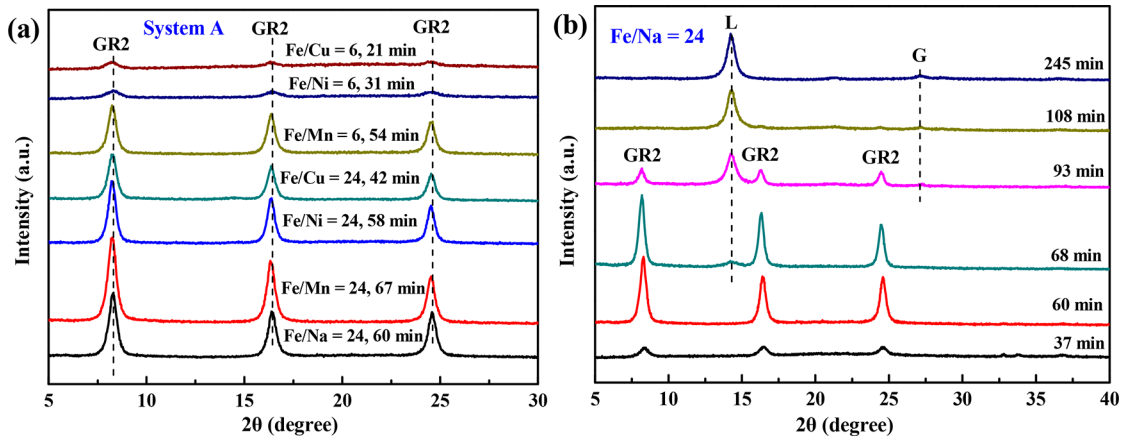

Figure 2. Fast-scanning XRD patterns of GR2 formed in the presence of different concentrations of foreign metal cations (a), and evolution of XRD patterns for the control system (Fe/Na = 24) as a function of time (b). GR2, hydrosulfate green rust; L, lepidocrocite; G, goethite.

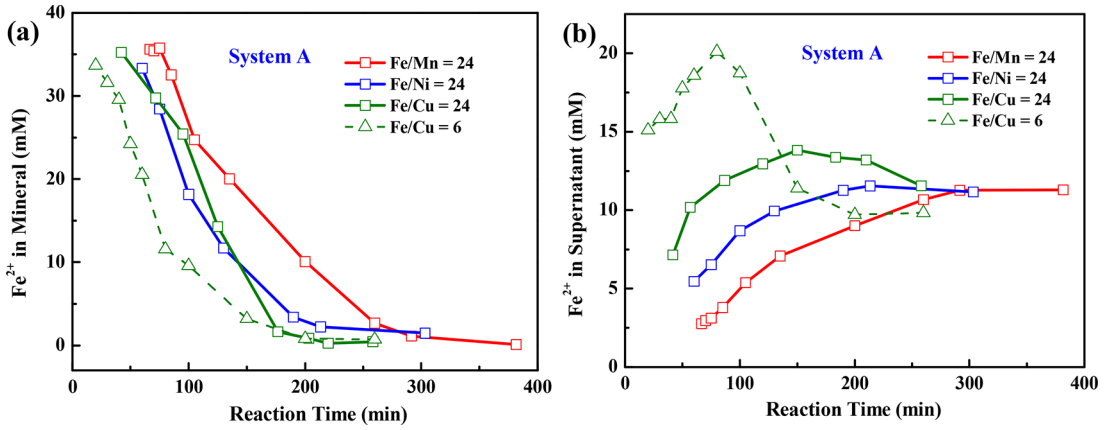

Figure 3. Variation of Fe^{2+} content in the minerals (a) and the dissolved Fe^{2+} (b) during the transformation of GR2 in the presence of Mn^{2+}, Ni^{2+}, or Cu^{2+} for the system A, the first point at each condition corresponds to the time when GR2 was formed completely.

slight decrease during GR2 transformation because of the release of some Fe^{2+} from the minerals (Figure 1b). Both the suspension pH and Eh curves show two obvious inflection points, corresponding to the complete formation of GR2 and to its complete transformation to Fe (hydr)oxides, respectively. Additionally, the Cu^{2+} system shows a third inflection point (indicated by green arrows).

At the formation stage of GR2 with Fe/Me^{2+} = 24 or 6 (Figure 1), the formation rate of GR2, determined from the time needed to reach the first inflection point of the suspension pH curve, in the presence of different cations decreases in the order of Cu^{2+} > Ni^{2+} > Mn^{2+}. Compared to the Na^{+} system, the low Mn^{2+} concentration (Fe/Mn = 24) delays the formation of GR2, while other studied conditions all accelerate the reaction; the higher cation concentration has a faster reaction rate. At the transformation stage of GR2 (Figure 1), the effects of cation type and concentration are similar to those at the formation stage, i.e., the transformation rate follows the order of Cu^{2+} > Ni^{2+} > Mn^{2+} and the higher cation concentration leads to a faster transformation.

For system B (Figure S1), cations are added once GR2 formation was complete and the product was stabilized by purging with N_2 for ∼40 min. Similar to system A, the transformation rate of GR2 in the presence of different cations with Fe/Me^{2+} = 24 follows the order of Cu^{2+} > Ni^{2+} > Mn^{2+}. For Fe/Me^{2+} = 6, the transformation rate decreases in the order of Cu^{2+} > Ni^{2+} ≈ Mn^{2+}.

XRD Patterns of the Intermediate Products. For system A, XRD patterns of intermediate products are shown in Figures 2b and S2. For the control system (Figure 2b), GR2 formation is complete at ∼60 min; during its subsequent transformation, the intensity of the diffraction peak of GR2 gradually decreases, and characteristic peaks of lepidocrocite appear at ∼68 min; and GR2 is completely converted into a mixture of lepidocrocite and goethite at ∼108 min. In the presence of Mn^{2+} (Figures S2a,b), the formation time of GR2 increases, although this time decreases with increasing Mn^{2+} concentration. During the transformation of GR2, lepidocrocite appears at ∼105 and ∼90 min, respectively, for Fe/Mn = 24 and 6, which is later than for the control system (∼68 min), indicating that Mn^{2+} increases GR2 stability. Additionally, the presence of Mn^{2+} hampers the crystallization of reaction products and formation of goethite but promotes the formation of lepidocrocite (Figures 2b and S2a,b). In both Ni^{2+} and Cu^{2+} systems (Figure S2c–f), GR2 also transforms into goethite and lepidocrocite; with increasing Ni^{2+} or Cu^{2+} concentration, the formation and transformation rates of GR2 gradually increase. For Fe/Cu^{2+} = 6 (Figure S2f), a minor goethite impurity forms together with GR2. At the high Ni^{2+} or Cu^{2+} concentration (Fe/Cu^{2+} = 6, Figure S2d,f), the fast

DOI: 10.1021/acsearthspacechem.8b00187
ACS Earth Space Chem. 2019, 3, 519−530

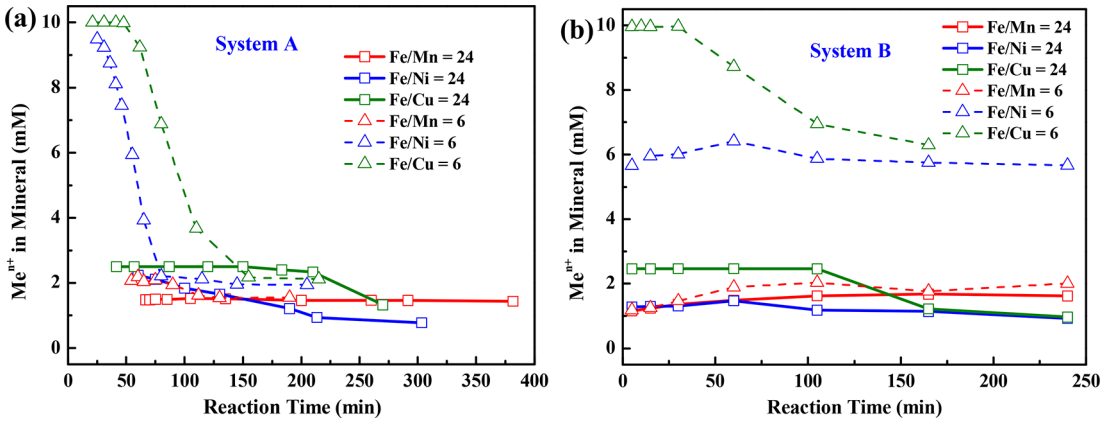

Figure 4. Cation content in the minerals during the transformation of GR2 in the presence of Mn^{2+}, Ni^{2+}, or Cu^{2+} for system A with the cations added at the beginning (a) and system B with the cations added after GR2 formation followed by N_2 purging (b). The first data point of each condition in system A corresponds to the time when GR2 formation was complete. System B was started upon the addition of the cations. The initial cation concentrations for Fe/Me^{2+} = 24 and 6, respectively, are 2.5 and 10 mM; note that the molar concentration of "mM" was used to represent the cation quantity in minerals because the mineral concentration cannot be accurately determined and constantly changes with reaction time.

formation and transformation of GR2 leads to poorly crystalline GR2 and transformation products.

The XRD patterns of GR2 obtained from different experimental conditions (Figure 2a) indicate that, compared to the control (Na^+) system, basal 00λ reflections of GR2 formed in the presence of cations slightly shift to low 2θ angles. Additionally, the presence of a high concentration of Cu^{2+} or Ni^{2+} significantly inhibits the crystallization of GR2, as indicated by the major broadening of these reflections.

For system B, compared with the control system (Na^+) (Figure S3), the transformation of GR2 in the presence of Mn^{2+} or Ni^{2+} is essentially similar (Figure S4a–d), with only a slight increase of GR2 peak intensities in the initial stages, suggesting that addition of Mn^{2+} or Ni^{2+} promotes the initial crystal growth of GR2. In contrast, the presence of Cu^{2+} results in a rapid decrease of GR2 peak intensity (Figure S4e,f), especially for Fe/Cu = 6 where the diffraction peaks of GR2 vanished after reacting for 15 min.

Fe^{2+} in the Minerals and Dissolved Fe^{2+} during the Formation and Transformation of GR2. For system A, at the first inflection point of the suspension pH curve, which corresponds to the complete formation of GR2, the Fe^{2+} content in the mineral (Figure 3a) is slightly lower than its theoretical Fe^{2+}/Fe_{total} = 2/3[41] (~40 mM, see the first point of Figure S5a). This lower Fe^{2+} content in GR2 may be due to the replacement of some Fe^{2+} by Mn^{2+}, Ni^{2+}, or Cu^{2+} cations. Meanwhile, when GR2 formation is complete, the soluble Fe^{2+} decrease in the order of Cu^{2+} > Ni^{2+} > Mn^{2+}, with a higher Cu^{2+} concentration resulting in a higher soluble Fe^{2+} (Figures 3b and S5b). During the following GR2 transformation, as the suspension pH continues decreasing, GR2 experiences a process of dissolution–oxidation–precipitation, releasing Fe^{2+} simultaneously, thus the soluble Fe^{2+} in both Ni^{2+} and Mn^{2+} systems gradually increases. However, in the Cu^{2+} system, the soluble Fe^{2+} first increases and then decreases, which is probably because when GR2 transforms completely the suspension pH of the Cu^{2+} system (~pH 4.7) is higher than those of the Ni^{2+} and Mn^{2+} systems (~pH 4.0), so that part of soluble Fe^{2+} oxidation continues, leading to the decrease of both soluble Fe^{2+} (Figures 3b and S5b) and suspension pH (Figures 1a and S1a) at the later stage. Additionally, the average oxidation rate of Fe^{2+} in the minerals decrease in the order of Cu^{2+} > Ni^{2+} > Mn^{2+}, and a higher Cu^{2+} concentration results in a faster Fe^{2+} oxidation rate (Figures 3a and S5a), consistent with the analysis of the pH/Eh curves (Figure 1).

Cation in the Minerals during the Formation and Transformation of GR2. For the system A, due to the high suspension pH at the initial stage (~pH 8.5), the rapid oxidation–hydrolysis–coprecipitation of Fe^{2+} and cations leads to the formation of cation-enriched GR2. When the GR2 formation is complete, the amount of cation entering the mineral decreases in the order of Cu^{2+} > Ni^{2+} > Mn^{2+}, with almost all added Cu^{2+} and Ni^{2+} being incorporated into the minerals (Figure 4a); this order is consistent with their hydrolysis constant [Cu^{2+} (pK_1 = 7.34) > Ni^{2+} (pK_1 = 9.86) > Mn^{2+} (pK_1 = 10.59)],[42] i.e., the more hydrolyzable cation is more readily to be adsorbed and coprecipitated. In addition, a higher initial cation concentration has more cation incorporated into the minerals, due to the greater driving force for adsorption and the lower pH that cation starts to precipitate. Subsequently, during the GR2 transformation, i.e., the dissolution–oxidation–precipitation reaction, the suspension pH gradually decreases, causing the cations release from the minerals by desorption and dissolution reactions; a higher initial cation concentration releases more cations with a faster rate. Compared with the Cu^{2+} and Ni^{2+} systems, the Mn^{2+} release is the lowest, probably because Mn^{2+} is adsorbed on the surface of the intermediate products and subsequently gets oxidized to Mn(III) species,[43] that can easily incorporate into the structure of the minerals.

For the system B (Figure 4b), the variation of the cation content in the minerals with time shows some differences from those of system A. During the transformation of GR2 in system B (Figure 4b), the Mn or Ni content in the minerals slightly increases at the initial stage by adsorption, oxidation, or coprecipitation, and then slightly decreases caused by the decrease of suspension pH. In contrast, almost all Cu are accumulated in the minerals at the beginning and some release at the later stage. After the transformation of GR2 completes, the cation content in the minerals in system B is slightly higher than that in system A. For the final dried products, the

DOI: 10.1021/acsearthspacechem.8b00187
ACS Earth Space Chem. 2019, 3, 519–530

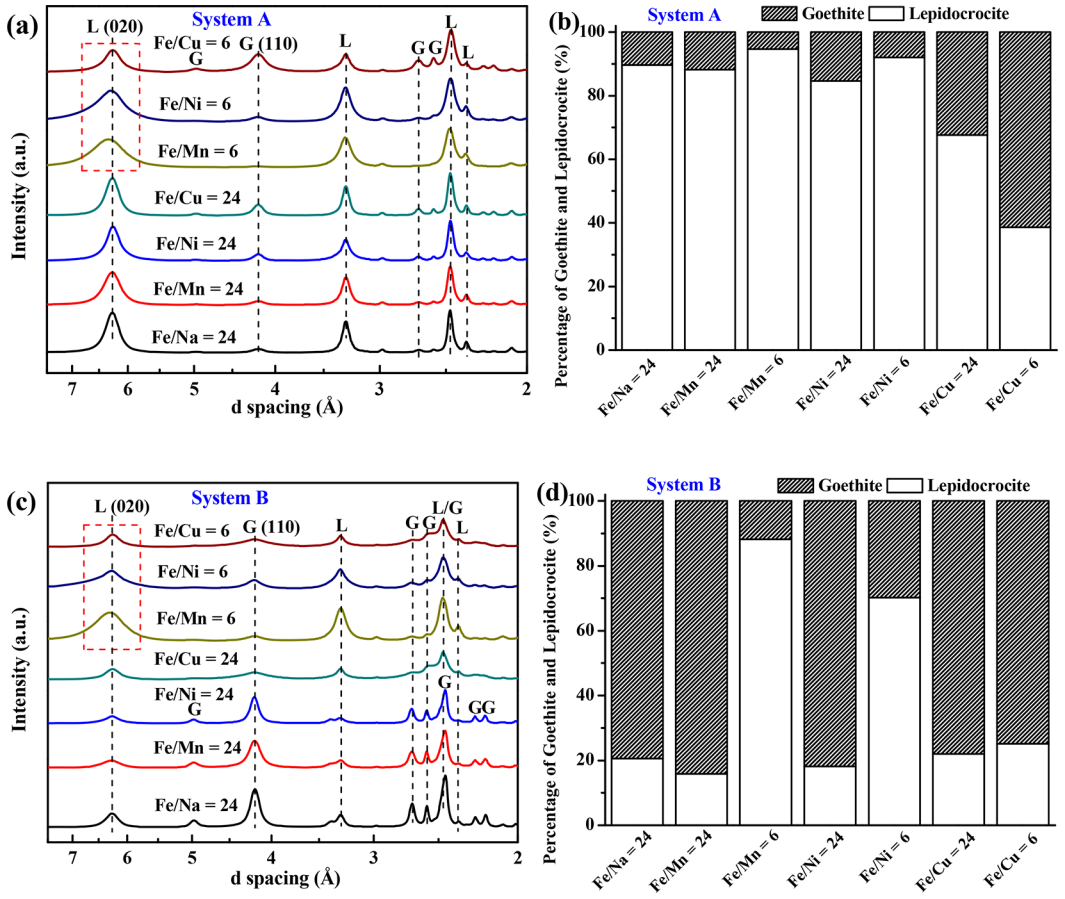

Figure 5. Synchrotron-based XRD patterns of the final dried samples obtained from different conditions: system A (a) and system B (c) (L, lepidocrocite; G, goethite). The percentage of the lepidocrocite and goethite obtained from Rietveld quantitative analyses of the corresponding XRD patterns are, respectively, shown in b and d, and the fitting results are shown in Figure S6.

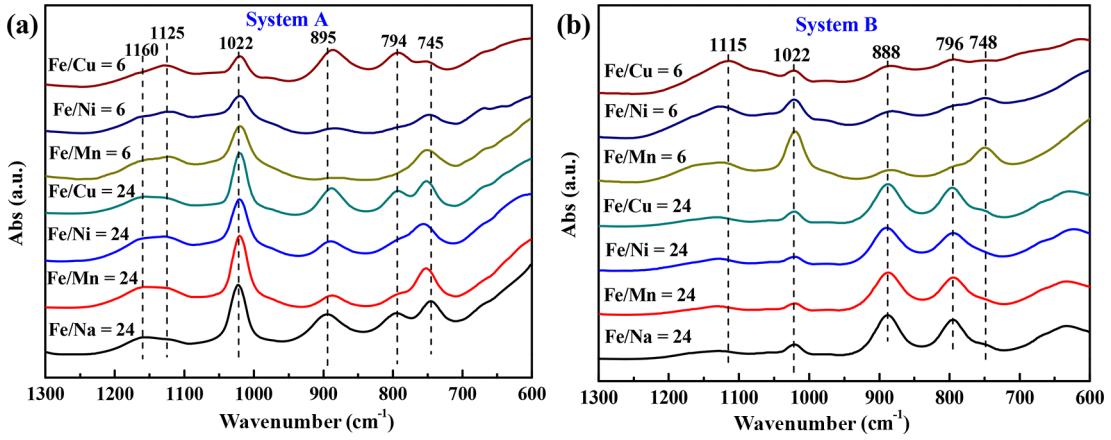

Figure 6. FTIR spectra of the final dried samples obtained from different conditions: system A to which cations were added at the beginning (a); and the system B to which cations were added after GR formation followed by purging N_2 for 40 min (b).

mineralogical properties and the speciation and spatial distribution of these cations were further characterized.

XRD Patterns and Their Quantitative Analysis of the Final Dried Samples. The XRD patterns and quantitative analysis of the final products (Figures 5 and S6) indicate that, under all conditions, the products are mixed phases of lepidocrocite and goethite with different crystallinity and relative proportion. For the system A (Figure 5a,b), the products are mainly lath-like lepidocrocite (Figure S7); compared with the control system, the presence of the cations inhibits the crystallization of lepidocrocite[5] (Figures 5a and S7). At Fe/Me^{2+} = 24, the shift of the diffraction peaks of lepidocrocite is insignificant, probably due to less isomorphous substitution of the cations; while at Fe/Me^{2+} = 6, more substitution of the cations causes the increase of (020) *d*-spacing value, and the magnitude of the increase decreases in the order of $Mn^{2+} > Ni^{2+} > Cu^{2+}$. In contrast, the presence of cations does not change the *d*-spacings of goethite but decreases its crystallinity and crystallite size (Figure 5a). The quantitative XRD analysis indicates that, at Fe/Me^{2+} = 24, the

DOI: 10.1021/acsearthspacechem.8b00187
ACS Earth Space Chem. 2019, 3, 519−530

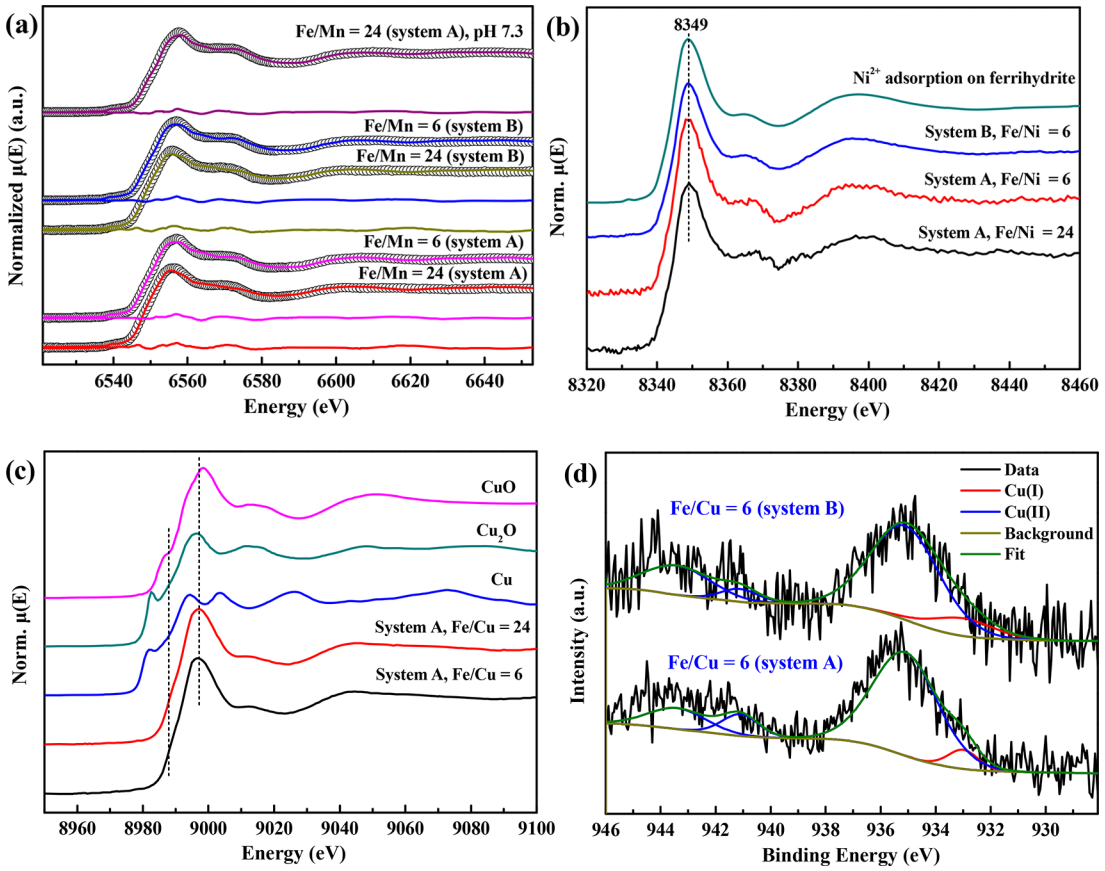

Figure 7. LCF fitting of Mn K-edge XANES spectra of the final dried samples of the Mn systems (circles are experimental data, lines are the linear combination best-fit with 17 references, difference plots are shown at the bottom of each spectra), and the fitted results were shown in Table 1 (a); Ni K-edge XANES spectra of part samples with Ni^{2+} adsorption on ferrihydrite as a comparison (b); Cu K-edge XANES spectra of part samples with Cu, Cu_2O, and CuO as comparison (c); the XPS Cu 2p spectra and their fits of the final dried samples of the Cu systems with Fe/Cu = 6 (d), and the fitted results are summarized in Table 1.

ratio of lepidocrocite to goethite (L/G) is similar to that of the control system; while at the higher Mn^{2+} or Ni^{2+} concentration (Fe/Me^{2+} = 6), the presence of Mn^{2+} or Ni^{2+} significantly promotes the formation of lepidocrocite (Figure 5b). In contrast, the ratio of L/G gradually decreases with the increase of Cu^{2+} concentration. For the pH effects at Fe/Mn = 24 (Figure S8), when the suspension pH during GR2 transformation was controlled at pH 7.3, more lepidocrocite is formed in the products.

For system B (Figure 5c,d), at Fe/Me^{2+} = 24, the products are mainly needle-like goethite (Figure S9), and the presence of the cations inhibits the crystallization of goethite, following the order of Cu^{2+} > Ni^{2+} > Mn^{2+} (Figure 5c); at Fe/Me^{2+} = 6, the crystallization of goethite is more significantly inhibited, while the crystallization of lath-like lepidocrocite is promoted to a certain degree. The substitution of cations also causes the peak shift of the (020) plane of lepidocrocite, consistent with the results of system A. The quantitative XRD analysis indicates that the high Mn^{2+}/Ni^{2+} concentration (Fe/Me^{2+} = 6) promotes the formation of lepidocrocite, consistent with the results of system A; in contrast, the effects of Cu^{2+} concentration are insignificant to the ratio of L/G (Figure 5d).

FTIR Spectra of the Final Dried Samples. The FTIR spectra of the samples obtained from system A and system B are depicted in Figure 6. The broad peak at wavenumber range of ~1050−1250 cm^{-1} belongs to the vibrational absorption of SO_4 adsorbed on iron oxide surfaces;[44] with the increase of the cation concentration, the relative intensity of peaks at 1160 to 1125 cm^{-1} decrease, suggesting the change of sulfate speciation on mineral surfaces. The bands at 1022 and 745 cm^{-1} belong to the OH bending vibration in and out of the (020) plane of lepidocrocite,[45] respectively, indicating the formation of lepidocrocite. Meanwhile, the bands at 888 and 794 cm^{-1} belong to the OH bending vibration of goethite,[46] respectively, indicating the formation of goethite. The infrared peak intensity and peak area can be generally used to semiquantify the content of different components;[47] the relative peak intensity/area of the characteristic peaks of lepidocrocite to goethite follows the order of Mn^{2+} > Ni^{2+} > Cu^{2+}, and higher cation concentration has a smaller relative proportion of lepidocrocite, basically consistent with the XRD analysis. Compared with the blank system, the vibration bands of 1022 and 895 cm^{-1} in the presence of cations shift to a low wavenumber, and the vibration peak of 745 cm^{-1} shifts to a high wavenumber, suggesting that the isomorphous substitution of cations occurs in both lepodocrocite and goethite structure.[48] In addition, the intensity and area of SO_4^{2-} vibration bands increase with increasing cation concentration, especially for system B, indicating that cations promotes SO_4^{2-} adsorption probably by forming a cation−sulfate ternary complex on mineral surface.[49]

XAS and XPS Spectroscopy of Selected Dried Samples. The LCF analysis of Mn K-edge XANES spectra indicates that the Mn species in the final products are mainly

DOI: 10.1021/acsearthspacechem.8b00187
ACS Earth Space Chem. 2019, 3, 519−530

Mn(III) with minor Mn(II) without Mn(IV) (Figure 7a and Table 1). With increasing Mn^{2+} concentration, more Mn(III) exist in the minerals (Figure 7a and Table 1), which might be caused by the stronger autocatalytic oxidation of Mn^{2+} at the higher Mn^{2+} concentration.[43] For the system B, the Mn AOS of the final products is slightly higher than that of system A, probably because more Mn^{2+} adsorbed on the mineral surfaces in system B, which is more favorable to the Mn(II) oxidation by interfacial catalysis, leading to a higher proportion of Mn(III). For the system A, when the suspension pH was controlled at 7.3 during GR2 transformation, all Mn in the minerals are Mn(III) because higher pH facilitates the Mn^{2+} oxidation.[50]

Table 1. Fitted Results of Mn and Cu Species Derived from Fitting of Mn K-Edge XANES Spectra and Cu 2p Spectra, Respectively

Mn system	Mn(II) (%)	Mn(III) (%)	AOS
Fe/Mn = 24 (system A)	37.7	62.3	2.62
Fe/Mn = 6 (system A)	14.0	86.0	2.85
Fe/Mn = 24 (system B)	31.4	68.6	2.69
Fe/Mn = 6 (system B)	6.6	93.4	2.93
Fe/Mn = 24 (system A)-pH 7.3	0	100	3.00
Cu system	Cu(I) (%)	Cu(II) (%)	
Fe/Cu = 6 (system A)	6.5	93.5	
Fe/Cu = 6 (system B)	11.6	88.4	

For the Ni system, Ni K-edge XANES spectra of the final samples are very similar to that of Ni^{2+} adsorbed on ferrihydrite surface (Figure 7b), indicating that the oxidation state of Ni does not change during the formation and transformation of GR2. For the Cu systems, Cu K-edge XANES spectra (Figure 7c) shows that the Cu species in the final products is more close to Cu(II) standard, suggesting Cu mainly exists as Cu(II) probably mixed with minor Cu(I). This is also confirmed by the Cu 2p XPS spectra analysis (Figure 7d). Compared to system A with Cu^{2+} added at the beginning, a little more Cu(I) was formed in system B with Cu added after GR2 formation (Table 1), which might be related to more Cu^{2+} adsorbed on the GR2 surface, thus facilitating the reaction between Cu(II) and Fe(II).

Acidic Dissolution Kinetics. The acidic dissolution kinetics of the final products can reflect the spatial distribution, crystallinity of minerals, and release rate of the cations from the minerals. The release kinetics of dissolved Fe can be described well with a pseudo first order equation (Figure S10). The obtained dissolution rate constant (k) at unit time are related to the crystallinity of the minerals and the relative proportion of lepidocrocite to goethite in the final products, with a higher crystallinity of minerals and/or a lower L/G ratio resulting in a lower dissolution rate (Table S1).

The dissolution ratio curve of divalent cation to Fe shows three shapes, i.e., convex, concave, and straight line with a slope close to 1. The convex curve indicates that the cations are mainly adsorbed on the mineral surface or form surface

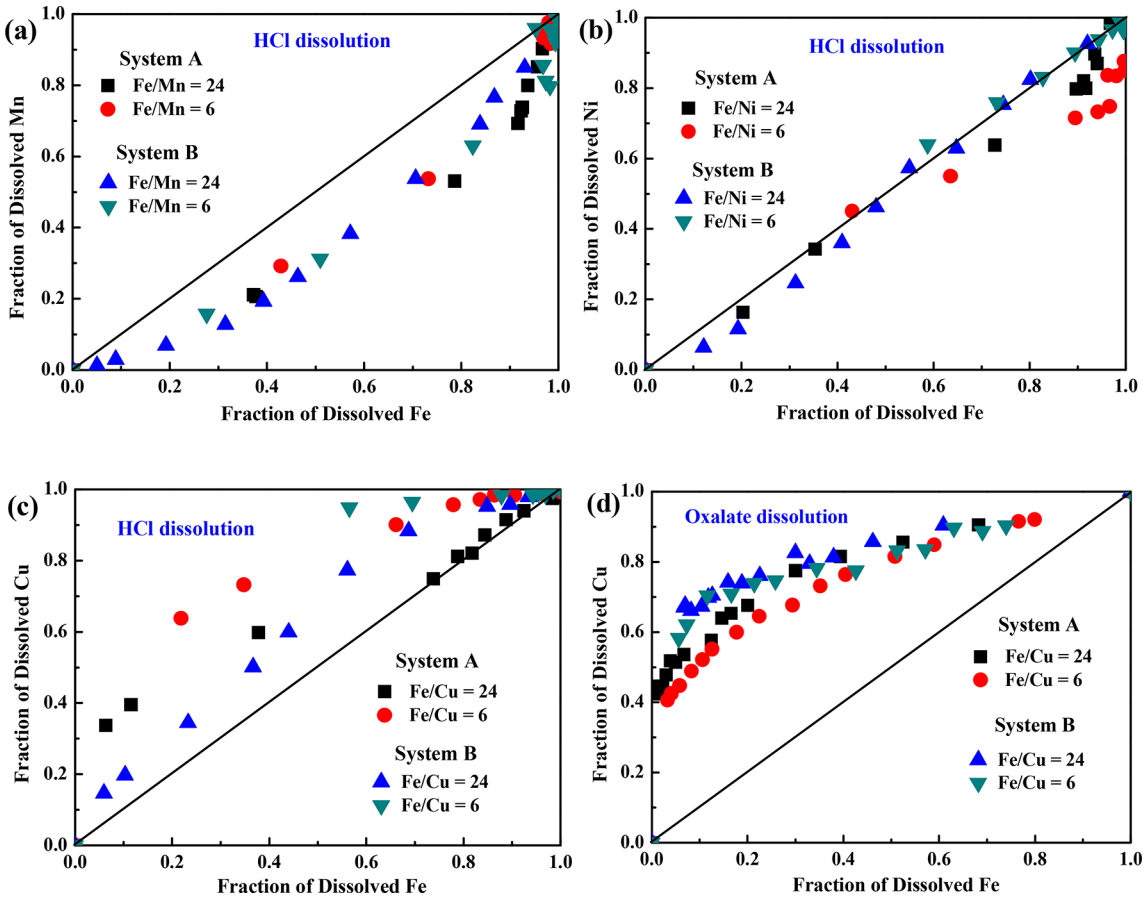

Figure 8. Release proportion of cations with the fraction of dissolved Fe for the final dried samples dissolved in 4 M HCl solution (a, Mn system; b, Ni system; c, Cu system) and 0.2 M acidic $(NH_4)_2C_2O_4$ solution (d, Cu system).

DOI: 10.1021/acsearthspacechem.8b00187
ACS Earth Space Chem. 2019, 3, 519−530

precipitates; the concave curve means that the cations are mainly distributed in the interior of minerals; the straight line means that the cations are uniform distributed in the minerals.[37,51] For the Mn system, the dissolution rate curve in the HCl solution appears concave (Figure 8a), indicating that Mn is mainly located inside the structure through isomorphous substitution and/or few precipitates (low valence Mn minerals) incorporated into the crystals. For the Ni system (Figure 8b), the dissolution rate curve in the HCl solution generally coincides with a straight line passing through the origin with a slope of 1, indicating that Ni is uniformly distributed in the mineral structure. For the Cu system, the dissolution rate curves in both HCl (Figure 8c) and oxalate (Figure 8d) solutions are all convex, indicating that Cu is mainly concentrated on the (sub)surface of the minerals and preferentially dissolved with respect to Fe.

DISCUSSION

Formation and Transformation of GR2 in the Presence of Cations. The first inflection point of the pH curve indicates the complete GR2 formation, whereas the second one indicates the complete GR2 transformation to Fe (hydr)oxides (Figure 1a). The formation of GRs by air oxidation usually consists of two processes:[52] the Fe(II) suspension is oxidized to form soluble $Fe^{II}_2Fe^{III}$ complexes; once these species reach oversaturation, GR2 then starts to form as described globally by the following equation:

$$5Fe^{II}(OH)_2 + Fe^{2+} + SO_4^{2-} + (1/2)O_2 + H_2O \leftrightarrow Fe^{II}_4Fe^{III}_2(OH)_{12}SO_4 \quad (1)$$

The presence of Fe(II) during the whole reaction process most likely induces the production of reactive oxygen species (ROS) by activating dissolved molecular O_2;[53] thus, the ROS should be one type of the oxidants responsible for the formation and transformation of GR2. When divalent cations are present in the initial solution, they may be structurally incorporated in GR2 through oxidation−hydrolysis−precipitation with Fe^{2+}, by occupying some Fe^{2+} sites in the GR2 structure (Figure 9),[54] resulting in a slightly increase of the d_{001} value of GR2. Additionally, the crystallinity of GR2 is significantly inhibited by high concentrations of Ni^{2+} or Cu^{2+} (Figure 2a) because most Ni^{2+} or Cu^{2+} enter the mineral at the GR2 formation stage (Figure 4a); in contrast, the effect of Mn^{2+} remains weak because the amount of Mn^{2+} in the mineral is relatively low (Figure 4a).

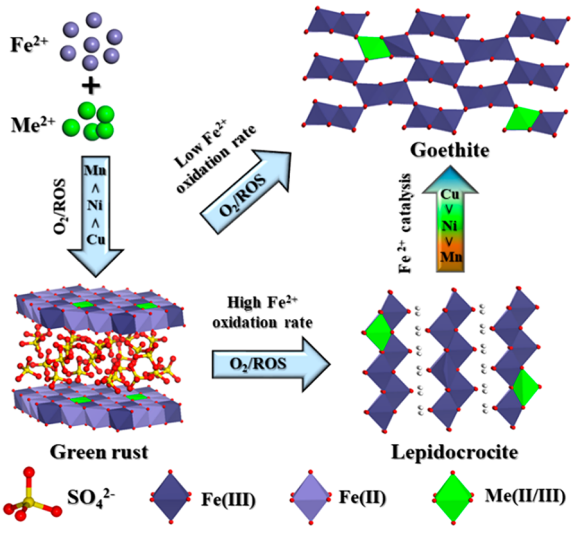

Figure 9. Schematic diagram of the formation and transformation of GR2 in the presence of foreign metal cations.

The formation and transformation rates of GR2 follow the order of Cu^{2+} > Ni^{2+} > Mn^{2+} (Figure 1), consistent with their hydrolysis constants, standard redox potentials (0.34, −0.257, and −1.17 V for Cu^{2+}/Cu, Ni^{2+}/Ni, and Mn^{2+}/Mn),[42] and surface complexation constants (for instance, the log K values of cation adsorption on ferrihydrite are 0.6 for Cu^{2+}, −2.5 for Ni^{2+}, and −3.5 for Mn^{2+}).[55] A cation with a stronger oxidation ability or a larger hydrolysis constant and complexation constant thus facilitates the formation and transformation of GR2. Moreover, a third inflection point occurs in the pH curve in the presence of Cu^{2+} (Figure 1a). This additional point may be linked to the higher suspension pH in the Cu^{2+} system after GR2 transformation that could lead to continuous oxidation of dissolved Fe^{2+}.

For system A and compared to the control system, the formation and transformation rates of GR2 decrease in the Mn^{2+} system at Fe/Mn = 24 and slightly increase at Fe/Mn = 6 (Figure 1). This dual behavior is possibly due, on the one hand, to the likely competition between Mn^{2+} and mineral surface sites for dissolved O_2, Mn^{2+} oxidation consuming some dissolved O_2 and thus inhibiting the formation and transformation of GR2; on the other hand, Mn(III) species formed from Mn(II) oxidation possess a strong oxidation capability,[50] thereby promoting the formation and transformation of GR2. At low Mn^{2+} concentration, the first effect likely prevails thus inducing an inhibitory effect, while high Mn^{2+} concentration plays a promoting role due to abundance of Mn(III) species (Figure 7a and Table 1).

In contrast, Ni^{2+} and Cu^{2+} both accelerate the formation and transformation of GR2 compared to the control system, the effect being more significant at higher metal concentration. The catalytic effect of Ni^{2+} is likely related to its fast hydrolysis effects (hydroxylation) that favor the hydrolysis−oxidation−coprecipitation reaction of Fe^{2+}/Fe^{3+},[56] and thus the formation and transformation of GR2. In addition to this fast hydrolysis effects, the presence of Cu^{2+} likely induces the production of OH· that enhances Fe^{2+} and GR2 oxidation, through the reaction between Cu(I), produced from the reduction of Cu(II), and dissolved O_2.[57,58]

For system B (Figure S1), the transformation rates of GR2 differ significantly for Mn^{2+} and Ni^{2+} systems at Fe/Me^{2+} = 24 (Ni^{2+} > Mn^{2+}) and Fe/Me^{2+} = 6 (Ni^{2+} ≈ Mn^{2+}). This is likely because the higher Mn concentration favors the formation of Mn(III) species that oxidize GR2. Similar to system A, a higher cation concentration results in a faster transformation (Figure 1).

Effects of Cation on the Transformation Products of GR2. Under all conditions, the final product of Fe(II) oxidation is a mixture of goethite and lepidocrocite, the proportions of which depend on the specific reaction conditions (Figure 9). The relative proportion of goethite in the presence of different cations decreases in the order of Cu^{2+} > Ni^{2+} > Mn^{2+} (Figure 5a−d). The formation of goethite is thus promoted by the presence of Cu^{2+}, i.e., a higher oxidation rate of Fe^{2+} in the minerals, which is contrary with goethite formation at a lower Fe^{2+} oxidation rate than lepidocrocite.[16] The reason might be related to the catalytic effect of surface

DOI: 10.1021/acsearthspacechem.8b00187
ACS Earth Space Chem. 2019, 3, 519−530

Fe^{2+}. The formation of lepidocrocite and/or goethite via GR2 transformation involves a dissolution−oxidation−crystallization mechanism (eq 2), and goethite is thermodynamically more stable than lepidocrocite.[59] During GR2 transformation to Fe (hydr)oxides, surface Fe^{2+} should follow the same order with soluble Fe^{2+}, i.e., Cu^{2+} > Ni^{2+} > Mn^{2+} (Figures 3b and S5b), because they keep dynamic balance with each other. Since the surface Fe^{2+} could catalyze the transformation of preformed lepidocrocite into goethite through continuous attachment and oxidation of Fe(II) by eq 3,[18,60,61] more goethite was formed in the presence of increasing Cu^{2+} concentration (Figure 5a,b). This suggests that Fe(II)-induced lepidocrocite transformation into goethite positively correlates with the complexation constant of cations, i.e., Cu^{2+} with a larger complexation constant leads to more goethite formation, similar to a previous report that cations with a larger complexation constant show a faster Fe(II)-induced dechlorination rate of trichloroethylene.[55]

$$Fe^{II}_4Fe^{III}_2(OH)_{12}SO_4 + (3/4)O_2 \leftrightarrow 5\alpha\text{-}Fe^{III}OOH/\gamma\text{-}Fe^{III}OOH + Fe^{2+} + SO_4^{2-} + (7/2)H_2O \quad (2)$$

$$5\gamma\text{-}Fe^{III}OOH + (Fe^{II})_{ads} + (1/4)O_2 + 2OH^- \xrightarrow{Fe^{II}\text{catalysis}} 6\alpha\text{-}Fe^{III}OOH + (1/2)H_2O \quad (3)$$

For the effect of Mn^{2+} and Ni^{2+} concentration, a higher Mn^{2+} or Ni^{2+} concentration (Fe/Me = 6) leads to the formation of more lepidocrocite (Figure 5b,d), especially for system A (Figure 5b), possibly because of the significant increase of GR2 formation and transformation rates (Figure 1), i.e., because of a higher Fe^{2+} oxidation rate. Similarly, more lepidocrocite is formed when the suspension pH is controlled at 7.3 because GR2 oxidation can be accelerated by the formation of more Mn(III) at higher pH values (Figure 7a and Table 1), promoting the formation of lepidocrocite.[16] Therefore, during the transformation of GR2 into lepidocrocite and goethite, both the Fe^{2+} oxidation rate and the catalytic effects of surface Fe^{2+} determine the mineralogical composition of the final products.

Speciation and Accumulation Mechanisms of Mn^{2+}, Ni^{2+}, and Cu^{2+} in Goethite and Lepidocrocite. In the final reaction products, Mn is mainly present as Mn(III) with minor Mn(II) (Figure 7a and Table 1), suggesting that Mn(III) substitutes for the structural Fe in the iron oxides, consistent with previous study.[51] In addition, dissolution experiments (Figure 8a) indicate that Mn concentration is higher in the inner parts of the minerals, suggesting the possible formation of minor Mn(II)/Mn(III) molecular clusters enclosed within the Fe (hydr)oxides crystals, which, however, cannot be identified by XRD. Moreover, a high Mn^{2+} concentration causes the increase of *d*-spacing of the (020) plane of lepidocrocite, possibly as the result of the structural incorporation of Mn(III).

For Ni system, the oxidation state of Ni is stable during the formation and transformation of GR2 (Figure 7b), and this cation is almost homogeneously distributed in the minerals (Figure 8b). For Cu system (Figure 7c,d), Cu is mainly present as Cu(II) in the final products with minor Cu(I), arising from Cu(II) reduction by Fe(II).[57,58] Acidic dissolution experiments indicate that Cu is mainly located on the edges of the minerals (Figure 8c,d), suggesting that the Cu(II) and Cu(I) species are mainly present on the surface of minerals.

Based on the speciation and distribution analysis of these three cations in goethite and lepidocrocite, they may be structurally incorporated in goethite and lepidocrocite (e.g., isomorphically substituted) in the order of Mn(III) > Ni(II) > Cu(II). This is likely induced by the similarity of their ionic radius, i.e., Fe(III) (0.65 Å) = Mn(III) (0.65 Å) < Ni(II) (0.69 Å) < Cu(II) (0.73 Å).

CONCLUSION

The presence of Mn^{2+}, Ni^{2+}, or Cu^{2+} significantly affects the formation and transformation processes of GR2 and underlying mechanisms, and the mineralogy of the final products. The cations with a larger hydrolysis constant and a higher redox potential (Cu^{2+} > Ni^{2+} > Mn^{2+}) exhibit faster GR2 formation and transformation rates and a higher amount of cation accumulated in the minerals, with a higher cation concentration more significant. Under all conditions, the final transformation product of GR2 is a mixture of lepidocrocite and goethite, the relative proportions depend on the oxidation rate of Fe^{2+} and the catalytic effects of surface Fe^{2+}. A slower Fe^{2+} oxidation rate and a stronger Fe^{2+} catalytic effect facilitate the formation of goethite. For these three cations, the preference for lepidocrocite formation follows the order of Mn^{2+} > Ni^{2+} > Cu^{2+}, and reverse order for the preferential goethite formation. In addition, isomorphic substitution of these three elements with the formed goethite and lepidocrocite follows the order of Mn(III) > Ni(II) > Cu(II). This provides new insights into the formation of goethite and lepidocrocite under different environmentally relevant conditions. Additionally, the cations of Mn, Ni, or Cu exhibit different distribution and chemical speciation in reaction final products, which will significantly change their microstructure and surface reactivity, thereby influencing their geochemical behaviors and the speciation and bioavailability of the associated heavy metals in soils and sediments.

ASSOCIATED CONTENT

Supporting Information

The Supporting Information is available free of charge on the ACS Publications website at DOI: 10.1021/acsearthspacechem.8b00187.

(1) Variation of suspension pH and Eh and Fe^{2+} in the minerals and in the solution for the system B, (2) XRD patterns of the intermediate products, (3) XRD Rietveld quantitative analyses and TEM images of the final products, and (4) kinetics of Fe release in HCl and the corresponding pseudo first order kinetic fitting (PDF)

AUTHOR INFORMATION

Corresponding Author

*E-mail: fxh73@mail.hzau.edu.cn.

ORCID

Xiaoming Wang: 0000-0002-5484-3922
Xiaoliang Liang: 0000-0001-6674-9354
Mengqiang Zhu: 0000-0003-1739-1055
Fan Liu: 0000-0003-0341-923X
Wenfeng Tan: 0000-0002-3098-2928
Xionghan Feng: 0000-0001-5499-7174

DOI: 10.1021/acsearthspacechem.8b00187
ACS Earth Space Chem. 2019, 3, 519−530

Notes

The authors declare no competing financial interest.

■ ACKNOWLEDGMENTS

We gratefully thank the National Natural Science Foundation of China (Nos. 41601228; 41471194), the China Postdoctoral Science Foundation (No. 2016M590700), and the Science and Technology Planning Project of Guangdong Province, China (2017B030314175) for their financial support. We acknowledge beamline scientists at Beamline 1W1B at Beijing Synchrotron Radiation Facility (BSRF) and at beamline 11-ID-B at the Advanced Photon Source (APS) for their assistance in data collection. This research used resources of APS, a DOE Office of Science User Facility, operated for the DOE Office of Science by Argonne National Laboratory under Contract DEAC02-06CH11357.

■ REFERENCES

(1) Christiansen, B. C.; Balic-Zunic, T.; Dideriksen, K.; Stipp, S. L. S. Identification of green rust in groundwater. *Environ. Sci. Technol.* **2009**, *43*, 3436−3441.

(2) Trolard, F. Fougerite: from field experiment to the homologation of the mineral. *C. R. Geosci.* **2006**, *338*, 1158−1166.

(3) Johnson, C. A.; Freyer, G.; Fabisch, M.; Caraballo, M. A.; Kusel, K.; Hochella, M. F. Observations and assessment of iron oxide and green rust nanoparticles in metal-polluted mine drainage within a steep redox gradient. *Environ. Chem.* **2014**, *11*, 377−391.

(4) Halevy, I.; Alesker, M.; Schuster, E. M.; Popovitz-Biro, R.; Feldman, Y. A key role for green rust in the precambrian oceans and the genesis of iron formations. *Nat. Geosci.* **2017**, *10*, 135.

(5) Dai, C.; Lin, M.; Hu, Y. Heterogeneous Ni- and Cd-bearing ferrihydrite precipitation and recrystallization on quartz under acidic pH condition. *ACS Earth Space Chem.* **2017**, *1*, 621−628.

(6) Refait, P.; Simon, L.; Genin, J. M. R. Reduction of SeO_4^{2-} anions and anoxic formation of iron(II)-iron(III) hydroxy selenate green rust. *Environ. Sci. Technol.* **2000**, *34*, 819−825.

(7) Trolard, F.; Bourrie, G.; Abdelmoula, M.; Refait, P.; Feder, F. Fougerite, a new mineral of the pyroaurite-iowaite group: description and crystal structure. *Clays Clay Miner.* **2007**, *55*, 323−334.

(8) Bernal, J. D.; Dasgupta, D. R.; Mackay, A. L. The oxides and hydroxides of iron and their structural inter-relationships. *Clay Miner.* **1959**, *4*, 15−30.

(9) Genin, J. M. R.; Bourrie, G.; Trolard, F.; Abdelmoula, M.; Jaffrezic, A.; Refait, P.; Maitre, V.; Humbert, B.; Herbillon, A. Thermodynamic equilibria in aqueous suspensions of synthetic and natural Fe(II)-Fe(III) green rusts: Occurrences of the mineral in hydromorphic soils. *Environ. Sci. Technol.* **1998**, *32*, 1058−1068.

(10) Ruby, C.; Usman, M.; Naille, S.; Hanna, K.; Carteret, C.; Mullet, M.; Francois, M.; Abdelmoula, M. Synthesis and transformation of iron-based layered double hydroxides. *Appl. Clay Sci.* **2010**, *48*, 195−202.

(11) Bond, D. L.; Fendorf, S. Kinetics and structural constraints of chromate reduction by green rusts. *Environ. Sci. Technol.* **2003**, *37*, 2750−2757.

(12) O'Loughlin, E. J.; Kelly, S. D.; Cook, R. E.; Csencsits, R.; Kemner, K. M. Reduction of uranium(VI) by mixed iron(II)/iron(III) hydroxide (green rust): formation of UO_2 manoparticies. *Environ. Sci. Technol.* **2003**, *37*, 721−727.

(13) O'Loughlin, E. J.; Burris, D. R. Reduction of halogenated ethanes by green rust. *Environ. Toxicol. Chem.* **2004**, *23*, 41−48.

(14) Schellenger, A. E. P.; Larese-Casanova, P. Oxygen isotope indicators of selenate reaction with Fe(II) and Fe(III) hydroxides. *Environ. Sci. Technol.* **2013**, *47*, 6254−6262.

(15) Legrand, L.; EL Figuigui, A.; Mercier, F.; Chausse, A. Reduction of aqueous chromate by Fe(11)/Fe(111) carbonate green rust: kinetic and mechanistic studies. *Environ. Sci. Technol.* **2004**, *38*, 4587−4595.

(16) Wang, X.; Liu, F.; Tan, W.; Feng, X.; Koopal, L. K. Transformation of hydroxycarbonate green rust into crystalline iron (hydr)oxides: influences of reaction conditions and underlying mechanisms. *Chem. Geol.* **2013**, *351*, 57−65.

(17) Wang, X.; Peng, J.; Xu, H.; Tan, W.; Liu, F.; Huang, Q.; Feng, X. Influences and mechanisms of As(V) concentration and environmental factors on hydrosulfate green rust transformation. *Acta Chim. Sinica* **2017**, *75*, 608−616.

(18) Feng, X.; Wang, X.; Zhu, M.; Koopal, L. K.; Xu, H.; Wang, Y.; Liu, F. Effects of phosphate and silicate on the transformation of hydroxycarbonate green rust to ferric oxyhydroxides. *Geochim. Cosmochim. Acta* **2015**, *171*, 1−14.

(19) Refait, P.; Reffass, M.; Landoulsi, J.; Sabot, R.; Jeannin, M. Role of phosphate species during the formation and transformation of the Fe(II-III) hydroxycarbonate green rust. *Colloids Surf., A* **2007**, *299*, 29−37.

(20) Benali, O.; Abdelmoula, M.; Refait, P.; Genin, J. M. R. Effect of orthophosphate on the oxidation products of Fe(II)-Fe(III) hydroxycarbonate: the transformation of green rust to ferrihydrite. *Geochim. Cosmochim. Acta* **2001**, *65*, 1715−1726.

(21) Christiansen, B. C.; Dideriksen, K.; Katz, A.; Nedel, S.; Bovet, N.; Sorensen, H. O.; Frandsen, C.; Gundlach, C.; Andersson, M. P.; Stipp, S. L. S. Incorporation of monovalent cations in sulfate green rust. *Inorg. Chem.* **2014**, *53*, 8887−8894.

(22) Choi, J.; Batchelor, B. Nitrate reduction by fluoride green rust modified with copper. *Chemosphere* **2008**, *70*, 1108−1116.

(23) O'Loughlin, E. J.; Kemner, K. M.; Burris, D. R. Effects of Ag^{I}, Au^{III}, and Cu^{II} on the reductive dechlorination of carbon tetrachloride by green rust. *Environ. Sci. Technol.* **2003**, *37*, 2905−2912.

(24) Choi, J. Y.; Batchelor, B.; Chung, J. W. Reductive dechlorination of tetrachloroethylene by green rusts modified with copper. *Water, Air, Soil Pollut.* **2010**, *212*, 407−417.

(25) Aissa, R.; Ruby, C.; Gehin, A.; Abdelmoula, M.; Genin, J. M. R. Synthesis by coprecipitation of Al-substituted hydroxysulphate green rust $(Fe_4^{II}Fe_{(2-y)}^{III}Al_y^{III}(OH)_{12}SO_4, nH_2O$. *Hyperfine Interact.* **2004**, *156*, 445−451.

(26) Refait, P.; Sabot, R.; Jeannin, M. Role of Al(III) and Cr(III) on the formation and oxidation of the Fe(II-III) hydroxysulfate green rust. *Colloids Surf., A* **2017**, *531*, 203−212.

(27) Inoue, K.; Kwon, S. K.; Kimijima, K.; Kanie, K.; Muramatsu, A.; Shinoda, K.; Suzuki, S.; Waseda, Y. Analysis of iron oxyhydroxides and oxides converted from green rust in aqueous solution. *ISIJ Int.* **2007**, *47*, 453−457.

(28) Yu, H.; Li, F.; Liu, C.; Huang, H.; Liu, T.; Yu, W. Iron redox cycling coupled to transformation and immobilization of heavy metals: implications for paddy rice safety in the red soil of south china. *Adv. Agron.* **2016**, *137*, 279.

(29) Duan, C.; Fang, L.; Yang, C.; Chen, W.; Cui, Y.; Li, S. Reveal the response of enzyme activities to heavy metals through in situ zymography. *Ecotoxicol. Environ. Saf.* **2018**, *156*, 106−115.

(30) Quantin, C.; Grunberger, O.; Suvannang, N.; Bourdon, E. Land management effects on biogeochemical functioning of salt-affected paddy soils. *Pedosphere* **2008**, *18*, 183−194.

(31) Johnson, C. A.; Murayama, M.; Kusel, K.; Hochella, M. F. Polycrystallinity of green rust minerals and their synthetic analogs: implications for particle formation and reactivity in complex systems. *Am. Mineral.* **2015**, *100*, 2091−2105.

(32) Genin, J. M. R.; Aissa, R.; Gehin, A.; Abdelmoula, M.; Benali, O.; Ernstsen, V.; Ona-Nguema, G.; Upadhyay, C.; Ruby, C. Fougerite and Fe^{II-III} hydroxycarbonate green rust; ordering drprotonation and/or cation substitution; structure of hydrotalcite-like compounds and mythic ferrosic hydroxide $Fe(OH)_{2+x}$. *Solid State Sci.* **2005**, *7*, 545−572.

(33) O'Loughlin, E. J.; Kelly, S. D.; Kemner, K. M.; Csencsits, R.; Cook, R. E. Reduction of Ag^{I}, Au^{III}, Cu^{II}, and Hg^{II} by Fe^{II}/Fe^{III} hydroxysulfate green rust. *Chemosphere* **2003**, *53*, 437−446.

(34) Ruby, C.; Abdelmoula, M.; Naille, S.; Renard, A.; Khare, V.; Ona-Nguema, G.; Morin, G.; Genin, J. M. R. Oxidation modes and thermodynamics of FeII-III oxyhydroxycarbonate green rust:

DOI: 10.1021/acsearthspacechem.8b00187
ACS Earth Space Chem. 2019, 3, 519−530

dissolution-precipitation versus in situ deprotonation. *Geochim. Cosmochim. Acta* **2010**, *74*, 953−966.
(35) Genin, J. M. R.; Ruby, C.; Gehin, A.; Refait, P. Synthesis of green rusts by oxidation of $Fe(OH)_2$, their products of oxidation and reduction of ferric oxyhydroxides; Eh-pH Pourbaix diagrams. *C. R. Geosci.* **2006**, *338*, 433−446.
(36) Hansen, H. C. B.; Borggaard, O. K.; Sorensen, J. Evaluation of the free energy of formation of Fe(II)-Fe(III) hydroxide-sulphate (green rust) and its reduction of nitrite. *Geochim. Cosmochim. Acta* **1994**, *58*, 2599−2608.
(37) Alvarez, M.; Rueda, E. H.; Sileo, E. E. Structural characterization and chemical reactivity of synthetic Mn-goethites and hematites. *Chem. Geol.* **2006**, *231*, 288−299.
(38) Wang, X.; Hu, Y.; Tang, Y.; Yang, P.; Feng, X.; Xu, W.; Zhu, M. Phosphate and phytate adsorption and precipitation on ferrihydrite surfaces. *Environ. Sci.: Nano* **2017**, *4*, 2193−2204.
(39) Wang, X.; Zhu, M.; Koopal, L. K.; Li, W.; Xu, W.; Liu, F.; Zhang, J.; Liu, Q.; Feng, X.; Sparks, D. L. Effects of crystallite size on the structure and magnetism of ferrihydrite. *Environ. Sci.: Nano* **2016**, *3*, 190−202.
(40) Manceau, A.; Marcus, M. A.; Grangeon, S. Determination of Mn valence states in mixed-valent manganates by XANES spectroscopy. *Am. Mineral.* **2012**, *97*, 816−827.
(41) Ruby, C.; Aissa, R.; Gehin, A.; Cortot, J.; Abdelmoula, M.; Genin, J. M. Green rusts synthesis by coprecipitation of Fe^{II}-Fe^{III} ions and mass-balance diagram. *C. R. Geosci.* **2006**, *338*, 420−432.
(42) Dean, J. A. *Lange's Handbook of Chemistry*, 15th ed.; McGrawHill: New York, 1999.
(43) Lan, S.; Wang, X.; Xiang, Q.; Yin, H.; Tan, W.; Qiu, G.; Liu, F.; Zhang, J.; Feng, X. Mechanisms of Mn(II) catalytic oxidation on ferrihydrite surfaces and the formation of manganese (oxyhydr)-oxides. *Geochim. Cosmochim. Acta* **2017**, *211*, 79−96.
(44) Beattie, D. A.; Chapelet, J. K.; Grafe, M.; Skinner, W. M.; Smith, E. In situ ATR-FTIR studies of SO_4 adsorption on goethite in the presence of copper ions. *Environ. Sci. Technol.* **2008**, *42*, 9191−9196.
(45) Lewis, D. G.; Farmer, V. C. Infrared absorption of surface hydroxyl groups and lattice vibrations in lepidocrocite (γ-FeOOH) and boehmite (γ-AlOOH). *Clay Miner.* **1986**, *21*, 93−100.
(46) Cambier, P. Infrared study of goethite of varying crystallinity and particle size. I. interpretation of OH and lattice vibration frequencies. *Clay Miner.* **1986**, *21*, 191−200.
(47) Xiao, W.; Jones, A. M.; Collins, R. N.; Bligh, M. W.; Waite, T. D. Use of fourier transform infrared spectroscopy to examine the Fe(II)-Catalyzed transformation of ferrihydrite. *Talanta* **2017**, *175*, 30−37.
(48) Cornell, R. M.; Schwertmann, U. *The Iron Oxides: Structure, Properties, Reactions, Occurrences and Uses*; Wiley-VCH: Weinheim, Germany, 2003.
(49) Zhang, G.; Peak, D. Studies of Cd(II)-sulfate interactions at the goethite-water interface by ATR-FTIR spectroscopy. *Geochim. Cosmochim. Acta* **2007**, *71*, 2158−2169.
(50) Lan, S.; Ying, H.; Wang, X.; Liu, F.; Tan, W.; Huang, Q.; Zhang, J.; Feng, X. Efficient catalytic As(III) oxidation on the surface of ferrihydrite in the presence of aqueous Mn(II). *Water Res.* **2018**, *128*, 92−101.
(51) Alvarez, M.; Sileo, E. E.; Rueda, E. H. Effect of Mn(II) incorporation on the transformation of ferrihydrite to goethite. *Chem. Geol.* **2005**, *216*, 89−97.
(52) Legrand, L.; Mazerolles, L.; Chausse, A. The oxidation of carbonate green rust into ferric phases: solid state reaction or transformation via solution. *Geochim. Cosmochim. Acta* **2004**, *68*, 3497−3507.
(53) Ona-Nguema, G.; Morin, G.; Wang, Y. H.; Foster, A. L.; Juillot, F.; Calas, G.; Brown, G. E. XANES evidence for rapid arsenic(III) oxidation at magnetite and ferrihydrite surfaces by dissolved O_2 via Fe^{2+}-mediated reactions. *Environ. Sci. Technol.* **2010**, *44*, 5416−5422.
(54) Genin, J. M. R.; Abdelmoula, M.; Ruby, C.; Upadhyay, C. Speciation of iron; characterisation and structure of green rusts and Fe^{II-III} oxyhydroxycarbonate fougerite. *C. R. Geosci.* **2006**, *338*, 402−419.
(55) Liu, T.; Li, X.; Waite, T. D. Depassivation of aged Fe-0 by divalent cations: correlation between contaminant degradation and surface complexation constants. *Environ. Sci. Technol.* **2014**, *48*, 14564−14571.
(56) Dai, C.; Hu, Y. Fe(III) hydroxide nucleation and growth on quartz in the presence of Cu(II), Pb(II), and Cr(III): metal hydrolysis and adsorption. *Environ. Sci. Technol.* **2015**, *49*, 292−300.
(57) Sun, Y.; Pham, A. N.; Waite, T. D. Effect of chloride driven copper redox cycling on the kinetics of Fe(II) oxidation in aqueous solutions at pH 6.5−8.0. *Geochim. Cosmochim. Acta* **2015**, *161*, 118−127.
(58) Stumm, W.; Lee, G. F. Oxygenation of ferrous iron. *Ind. Eng. Chem.* **1961**, *53*, 143−146.
(59) Navrotsky, A.; Mazeina, L.; Majzlan, J. Size-driven structural and thermodynamic complexity in iron oxides. *Geochim. Cosmochim. Acta* **2008**, *72*, A673−A673.
(60) Boland, D. D.; Collins, R. N.; Miller, C. J.; Glover, C. J.; Waite, T. D. Effect of solution and solid-phase conditions on the Fe(II)-accelerated transformation of ferrihydrite to lepidocrocite and goethite. *Environ. Sci. Technol.* **2014**, *48*, 5477−5485.
(61) Han, R.; Liu, T.; Li, F.; Li, X.; Chen, D.; Wu, Y. Dependence of secondary mineral formation on Fe(II) production from ferrihydrite reduction by shewanella oneidensis MR-1. *ACS Earth Space Chem.* **2018**, *2*, 399−409.

DOI: 10.1021/acsearthspacechem.8b00187
ACS Earth Space Chem. 2019, 3, 519−530